Chemical Science

ROYAL SOCIETY OF CHEMISTRY

EDGE ARTICLE

View Article Online
View Journal

Cite this: DOI: 10.1039/d5sc08430j

All publication charges for this article have been paid for by the Royal Society of Chemistry

Post-synthetic gridization enhances spin-flip dynamics, horizontal alignment, and ozone resistance in solution-processable TADF macrocycles

Quanyou Feng, [a] Aiyun Zhu,[a] Qiuhu Han,[a] Kewei Guo,[a] Yunfei Zhu,[a] Yue Cao,[a] Jingyao Ma,[a] Hao Li,[a] Hongjian Wang, [a] Yuyu Pan, *[b] Xinxin Ban, [c] Mengna Yu,[a] Man Xu,[a] Zilu Wang,*[a] Guohua Xie, [d] Linghai Xie *[ae] and Wei Huang*[aef]

Nanoemitters play a pivotal role in advancing OLED technologies toward flexible, efficient, and sustainable display platforms. However, current quantum dots and perovskite LEDs suffer from structural instability and environmental sensitivity, limiting their scalability. Here, we introduce a post-synthetic gridization strategy to construct robust, solution-processable organic nanodots. The resulting A-shaped nanogrid (AG) framework provides a rigid and sterically protected donor scaffold that suppresses aggregation-caused quenching, promotes horizontal dipole orientation and ozone resistance, and minimizes reorganization energy. Based on this design, the thermally activated delayed fluorescence (TADF) emitter AG-PXZ-TRZ exhibits a 3.1-fold enhancement in the radiative decay rate and a 5.5-fold acceleration of reverse intersystem crossing relative to the parent emitter PXZ-TRZ, together with an improved horizontal molecular orientation of 83%. Solution-processed OLEDs based on AG-PXZ-TRZ achieve an external quantum efficiency of 28.9%, markedly surpassing the performance of both PXZ-TRZ and the arylmethylated analogue DPFPXZ-TRZ. This work establishes molecular gridization as an effective pathway toward stable and high-performance organic nanoemitters for next-generation optoelectronic displays.

Received 31st October 2025
Accepted 20th January 2026

DOI: 10.1039/d5sc08430j

rsc.li/chemical-science

Introduction

The rapid evolution of light-emitting materials drives innovation across next-generation display technologies, ranging from printable flexible and stretchable devices for wearable applications to micro-LEDs enabling immersive AR/VR experiences within the metaverse.[1,2] Emerging platforms, such as smart sensor displays for multi-scenario detection, remote telecommunication interfaces, and vivid 3D holographic systems enhanced by machine learning, further underscore the demand for high-performance emitters.[3,4] Since the pioneering report on OLEDs by Tang in 1987,[5] OLED technology has successfully challenged the dominance of LCDs and achieved large-scale commercialization, with a global market value reaching USD 65.7 billion.[6] However, the high capital expenditure and the substantial energy consumption required for OLED fabrication limit broader scalability and raise critical concerns regarding environmental sustainability. In response, quantum dots (QDs) and hybrid perovskite LEDs have emerged as leading candidates for next-generation quantum nanoemitters, combining solution-processability with exceptional color purity and superior current-density-driven efficiency.[4,7] Despite these advantages, their practical implementation remains constrained by inherent structural imprecision, ligand coordination instability, and susceptibility to ambient processing environments.[8,9] These persistent challenges fuel an ongoing debate over the optimal technological trajectory, shaping the search for intelligent display systems that unite efficiency, scalability, and sustainability.

One creative technique route was initiated with organic nanodots for next-generation emitters beyond all the past

[a]Centre for Molecular Systems and Organic Devices (CMSOD), State Key Laboratory of Flexible Electronics, Institute of Advanced Materials (IAM), Nanjing University of Posts & Telecommunications, 9 Wenyuan Road, Nanjing 210023, P. R. China. E-mail: iamlhxie@njupt.edu.cn; iamzlwang@njupt.edu.cn

[b]School of Petrochemical Engineering, Shenyang University of Technology, 30 Guanghua Street, Liaoyang 111003, P. R. China. E-mail: panyu0422@sut.edu.cn

[c]School of Environmental and Chemical Engineering, Jiangsu Key Laboratory of Function Control Technology for Advanced Materials, Jiangsu Ocean University, 59 Cangwu Road, Lianyungang 222005, P. R. China

[d]The Institute of Flexible Electronics (Future Technologies), Xiamen University, 422 Siming South Road, Xiamen 361005, P. R. China

[e]School of Flexible Electronics (SoFE), Henan Institute of Flexible Electronics (HIFE), Henan University, 379 Mingli Road, Zhengzhou 450046, P. R. China

[f]Frontiers Science Center for Flexible Electronics (FSCFE), State Key Laboratory of Flexible Electronics, Northwestern Polytechnical University, 127 West Youyi Road, Xi'an 710072, China. E-mail: vc@nwpu.edu.cn

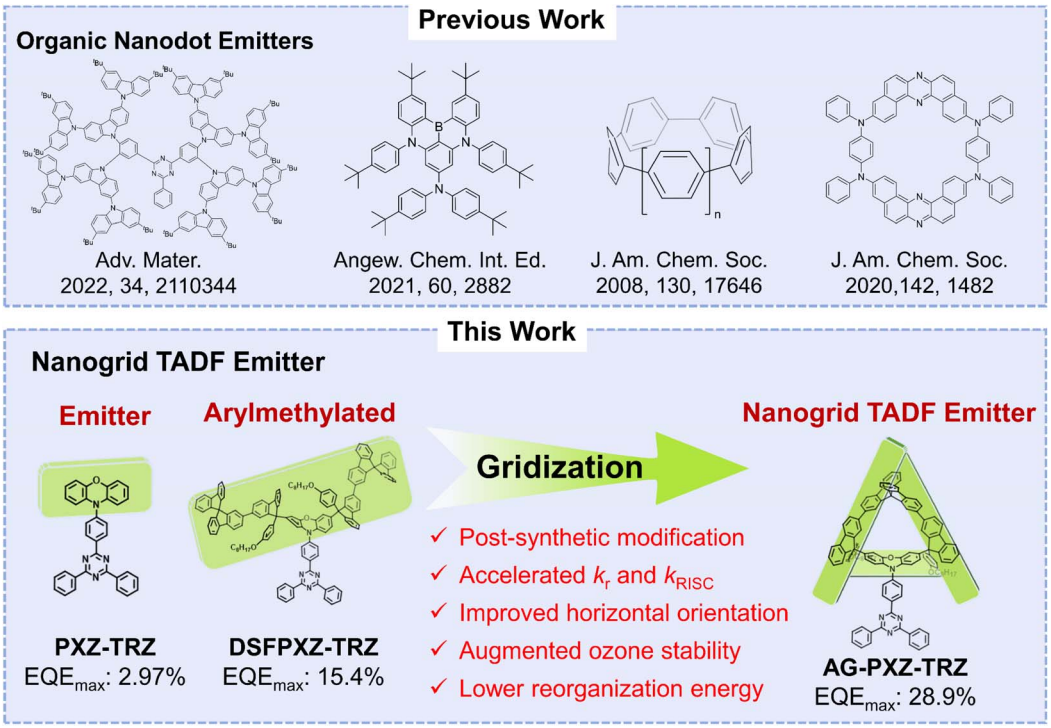

Fig. 1 Organic nanodot emitters and the molecular design concept in this work.

designs of exciton/photon-emissive materials.[10,11] Organic nanostructures such as dendrimers, fused aromatics, and macrocycles have attracted considerable interest in optoelectronic applications owing to their diverse structural advantages.[12–14] For example, as shown in Fig. 1a, dendrimers facilitate the self-encapsulation of emissive cores, effectively suppressing aggregation-caused quenching (ACQ) and enabling the realization of solution-processable, host-free emitters.[15] In parallel, fused aromatic systems,[16,17] particularly boron-nitrogen multi-resonance frameworks,[18,19] afford exceptionally narrowband emission, opening new avenues toward high-color-purity light-emitting materials. Moreover, organic macrocycles serve as a versatile molecular platform,[20–23] where strained cycloparaphenylenes enable tunable emission,[24,25] donor–acceptor architectures regulate p/n polarity,[22] and functionalized derivatives deliver fluorescence,[26,27] phosphorescence,[28,29] and TADF properties[22,30,31] positioning them as high-performance, solution-processable materials. Optimizing molecular design to minimize reorganization energy is crucial for stabilizing charge-transfer (CT) states of emitters.[32] Organic nanodots are emerging as promising candidates for next-generation quantum technologies, neuromorphic computing, and intelligent display systems.[11,33] Integrating advanced molecular engineering with modern chemical approaches offers a transformative pathway toward low-cost fabrication and ultrahigh market potential.

Compared with fused polycyclic aromatization, dendrimerization, and macrocyclization, molecular gridization enables the construction of zero-, one-, two-, and three-dimensional nanoscale architectures with distinct inorganic-like optoelectronic characteristics.[34] Friedel–Crafts gridization (FCG) establishes the foundational principles of gridization, providing state-of-the-art structural models and efficient nanosynthesis methodologies. In this context, nanogrids incorporating aromatic amines could be used as unique electronic donors for constructing interesting and efficient emitters with advantages in the following aspects (Fig. 1b). (i) The inherent rigidity of nanogrid's molecular framework effectively minimizes structural relaxation, thereby reducing reorganization energy,[35] while its robust architecture and effective blockade of the aromatic amine active sites significantly enhance thermal, chemical, and electrical stability.[36,37] (ii) The multiple steric hindrances of the nanogrids are beneficial to suppress the molecular interactions and thus prevent the ACQ effect, which further increase the photoluminescence quantum yield (PLQY) for luminescent materials.[38,39] (iii) Increased molecular weight and/or extended molecular backbones favour horizontal orientation of the emitters, thereby enhancing light outcoupling efficiency.[36,40] (iv) The incorporation of alkyl and alkoxyl groups at the 9-positions of fluorene units offers a straightforward strategy to improve solution processability and film-forming properties.[41,42]

Here, we present a post-synthetic gridization strategy that enables the construction of A-shaped nanogrid (AG) with high-yield synthesis, opening new pathways toward the scalable commercialization of organic nanodots for flexible electronics. Based on this design principle, we develop the nanogrid emitter AG-PXZ-TRZ through post-synthetic gridization of the TADF emitter PXZ-TRZ. We select PXZ-TRZ as the representative TADF emitter because phenoxazine–triazine donor–acceptor architectures are extensively studied and consistently deliver intriguing photophysical behaviour.[43–46] Building on the advantages mentioned above, AG-PXZ-TRZ, in comparison with

its parent compound PXZ-TRZ[47] and the arylmethylated analogue DSFPXZ-TRZ, exhibits suppressed aggregations, enhanced rates of reverse intersystem crossing (k_{RISC}) and radiative decay (k_r), an improved horizontal molecular orientation of up to 83%, greater ozone tolerance, and lower reorganization energy (Fig. 1b). When employed as a dopant in solution-processed OLEDs, AG-PXZ-TRZ consequently yields a substantial enhancement in electroluminescent performance, achieving an external quantum efficiency of 28.9%, which markedly exceeds that of devices based on PXZ-TRZ and DSFPXZ-TRZ.

Results and discussion

Molecular design and synthesis

The A-shaped nanogrid framework can be constructed using two fluorene units, a bridging group, and an arylamine electron donor. The bridging group connects to the fluorene units either through conjugated or non-conjugated linkages, while the arylamine is attached at the 9-position of the fluorene units, forming the characteristic A-shaped configuration. In this study, spirobifluorene was employed as the bridging moiety linked *via* conjugated bonds and a phenoxazine (PXZ) unit was utilized as the arylamine donor. First, we synthesized the difluorenol 2,2′-(9,9′-spirobi[fluorene]-2,2′-diyl)bis(9-(4-(octyloxy) phenyl)-9*H*-fluoren-9ol) (DOHSBF)[48] *via* a Suzuki coupling reaction. Subsequent reactions with the phenoxazine unit yielded the phenoxazine-based functionalized nanogrid. However, the low yield of the acid-catalyzed Friedel–Crafts gridization, attributed to the protonation susceptibility of the phenoxazine nitrogen under acidic conditions, hindered the preparation of nanogrid-functionalized emitters. To address this limitation, we synthesized another modified nanogrid, namely AG-EtPXZ, by incorporating ethyl-substituted phenoxazine. The chemical structure of AG-EtPXZ was confirmed through matrix-assisted laser desorption/ionization time of flight mass spectrometry (MALDI-TOF MS) and nuclear magnetic resonance (NMR) spectroscopy, demonstrating the feasibility of modifying the nanogrid with aromatic amine donors. Consequently, a post-synthetic gridization strategy was employed, as illustrated in Scheme S2 in the SI, enabling the efficient synthesis of AG-PXZ-TRZ *via* Friedel–Crafts arylmethylation of the TADF emitter PXZ-TRZ with DOHSBF, achieving a remarkable yield of up to 84%. The high yield, simplicity and universality underscore the robustness of this refined synthetic methodology. To investigate the gridization effect, its acyclic counterpart, DSFPXZ-TRZ, was also synthesized. Their chemical structures were definitely characterized by ^{1}H NMR, 2D NOESY NMR, ^{13}C NMR and mass spectrometry (Fig. S1–S7). The detailed synthetic methods are presented in the SI. The characteristic triplet at 3.82 ppm in

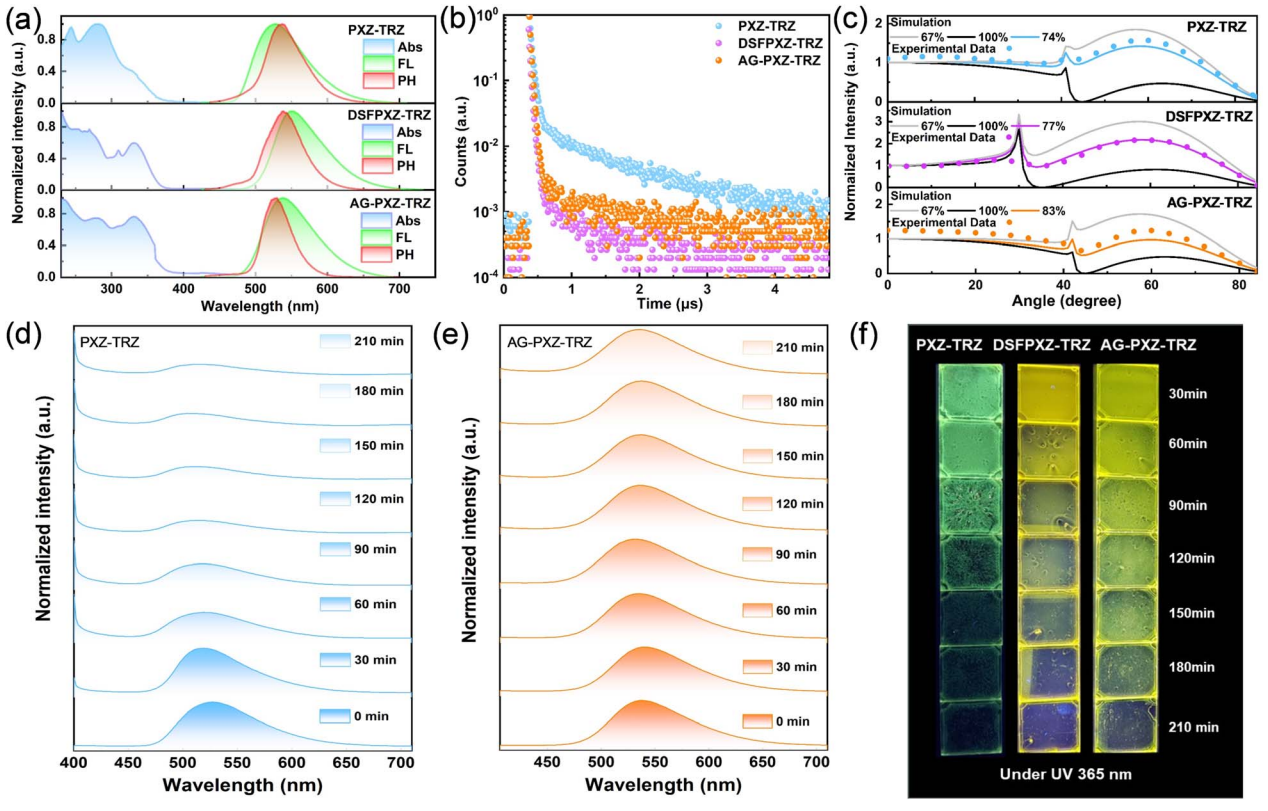

Fig. 2 (a) Normalized UV-vis absorption, room temperature fluorescence (298 K) spectra and low-temperature phosphorescent (77 K) spectra in the film state for PXZ-TRZ, DSFPXZ-TRZ, and AG-PXZ-TRZ. (b) Transient PL decay curves on 30 wt% emitters doped in the CBP host. (c) Measured p-polarized PL intensity (at the PL peak wavelength) of 30 wt% PXZ-TRZ, DSFPXZ-TRZ, and AG-PXZ-TRZ doped into CBP as a function of the emission angle. PL spectra of the (d) pristine PXZ-TRZ and (e) pristine AG-PXZ-TRZ films after various periods of ozone aging. (f) Photographs of the ozone aged polymer films.

Table 1 Physical data and kinetic parameters of the emitters

Emitter	λ_{em}[a] [nm]	E_{S_1}[b] [eV]	E_{T_1}[b] [eV]	ΔE_{ST} [eV]	Φ_{PL}[c] [%]	τ_p[d] [ns]	τ_d[d] [μs]	k_r[e] [10^7 s^{-1}]	k_{ISC}[e] [10^7 s^{-1}]	k_{RISC}[e] [10^6 s^{-1}]
PXZ-TRZ	527	2.17	1.90	0.27	68	11.8	1.14	1.46	7.02	0.36
DSFPXZ-TRZ	550	2.07	1.90	0.17	60	35.2	0.99	0.81	2.05	1.26
AG-PXZ-TRZ	538	2.10	1.94	0.16	77	9.19	1.03	4.55	6.33	2.00

[a] Measured in neat films. [b] Estimated from fluorescent and phosphorescent spectra in neat films. [c] Obtained from integrating sphere measurements for the 30 wt% doped CBP films. [d] Lifetime of prompt and delayed fluorescence. [e] Radiative decay rate (k_r) from S_1 to S_0 states, the intersystem crossing rate (k_{ISC}), and the reverse intersystem crossing rate (k_{RISC}).

the ^{1}H NMR spectrum suggests that AG-PXZ-TRZ possesses a high degree of symmetry, consistent with the presence of a C_2 symmetry axis. This observation indicates that the two $C_8H_{17}O$–Ph substituents adopt a *trans* configuration, as only this arrangement accounts for the observed spectral symmetry. Furthermore, the ^{1}H–^{1}H NOESY spectrum shows a clear NOE correlation between the resonances at 3.82 ppm and 6.7 ppm, supporting the conclusion that the $C_8H_{17}O$–Ph groups bend inward toward the molecular core (Fig. S6).

Exceptional thermal properties contribute significantly to the long-term stability and sustainability of solution-processed devices when deployed in real-world environments. Then the thermal properties of the emitter were examined using thermogravimetric analysis (TGA) and differential scanning calorimetry (DSC). As shown in Fig. S8, the decomposition temperatures (T_d, with 5% weight loss) of AG-PXZ-TRZ and DSFPXZ-TRZ are 236 °C and 305 °C, respectively. And the glass transition temperatures (T_g) of AG-PXZ-TRZ and DSFPXZ-TRZ are 183 °C and 202 °C, respectively. These thermal properties of AG-PXZ-TRZ enable it to undergo annealing treatment during solution processing, which is important for device fabrication and performance. In addition, the introduction of the nanogrid framework also enhances the solubility of the material, which guarantees efficient film forming through solution processing. The atomic force microscopy (AFM) measurement was employed to examine the film-forming capability and morphological characteristics of the solution-processed films. As shown in Fig. S10, the AFM images of parent emitter PXZ-TRZ reveal a significant surface roughness of 5.88 nm, marked by numerous cracks and crystalline structures. This observation suggests that PXZ-TRZ exhibits suboptimal film-forming properties. In contrast, AG-PXZ-TRZ and DSFPXZ-TRZ based films exhibit significantly reduced RMS values of 0.38 nm and 0.917 nm, respectively. The smooth and uniform morphology of the AG-PXZ-TRZ film, which is devoid of any pinholes, cracks, or crystalline inclusions, strongly indicates that high-quality films can be achieved *via* spin-coating using AG-PXZ-TRZ.

Photophysical properties

All three emitters in solution show a distinct vibronically structured absorption band below 350 nm, attributed to π–π* transitions, alongside a weaker absorption feature in the 350–500 nm range, characteristic of intramolecular charge-transfer (ICT) transitions from the phenoxazine donor to the triazine acceptor moiety (Fig. S11a). The PL spectrum of AG-PXZ-TRZ displays a broad emission band centered at 554 nm. Relative to the parent emitter PXZ-TRZ, DSFPXZ-TRZ displays a redshift of 23 nm, whereas AG-PXZ-TRZ shows a more modest shift of 9 nm. These redshifted emission peaks are ascribed to the enhanced electron-donating character conferred by arylmethyl substitution at the 3,6-positions. As shown in Fig. 2a and Table 1, AG-PXZ-TRZ exhibits a PL peak at 538 nm with a PLQY value of 77% in the solid-state film. The singlet energies of DSFPXZ-TRZ and AG-PXZ-TRZ, derived from the onset of their PL spectra, are 2.07 eV and 2.10 eV, respectively. Corresponding triplet energies, estimated from the highest-energy vibronic features of the phosphorescence spectra at 77 K, are 1.90 eV and 1.94 eV. These values yield an experimental ΔE_{ST} of 0.17 eV for DSFPXZ-TRZ and 0.16 eV for AG-PXZ-TRZ. These ΔE_{ST} values are much lower than those of the parent emitter PXZ-TRZ, indicating that the functionalized emitters facilitate more efficient reverse intersystem crossing (RISC) from non-radiative triplet states to the emissive singlet manifold.

The fluorescence decays of AG-PXZ-TRZ in the film state at room temperature were also monitored to explore their emissive characteristics. As illustrated in Fig. 2b, similar to the parent emitter PXZ-TRZ, the arylmethylated DSFPXZ-TRZ also clearly exhibits two component emission decays, consisting of a prompt component of 35.2 ns and delayed component of 0.99 μs. Following gridization, the emitter AG-PXZ-TRZ displays a delayed lifetime similar to that of its precursor, while demonstrating a significantly shorter prompt lifetime of 9.19 ns. The reduced delayed lifetime of AG-PXZ-TRZ can be attributed to its smaller ΔE_{ST}, which effectively enhances the RISC process while suppressing non-radiative decay from the triplet state. To further demonstrate the TADF properties, the oxygen sensitivity test was performed. As shown in Fig. S10b, the fluorescence is markedly quenched in the presence of oxygen, whereas a pronounced enhancement in delayed emission is observed upon N_2 bubbling, providing compelling evidence for the involvement of triplet states in the emissive process. It can be seen from Table 1 that arylmethylation leads to a notable increase in the k_{RISC}, from 0.36×10^6 s^{-1} for PXZ-TRZ to 1.26×10^6 s^{-1} for DSFPXZ-TRZ. Following gridization, the AG-PXZ-TRZ molecule displays a further reduced ΔE_{ST}, which consequently facilitates faster reverse intersystem crossing with a k_{RISC} of 2.00×10^6 s^{-1}. This enhancement likely correlates with spin–orbit coupling (SOC) between S_1 and the triplet states (as explored in the following Theoretical calculations section) and markedly improves the utilization of triplet excitons during electroluminescence. The radiative decay rate constants (k_r) are determined

to be 4.55 × 10^7 s^{-1}, 0.81 × 10^7 s^{-1} and 1.46 × 10^7 s^{-1} for AG-PXZ-TRZ, DSFPXZ-TRZ and PXZ-TRZ, respectively. The substantially increased k_{RISC} and k_r of AG-PXZ-TRZ effectively suppress non-radiative losses and curtail repeated spin-flip processes, which is critical in limiting the accumulation of triplet excitons. Consequently, these favourable exciton dynamics in AG-PXZ-TRZ are anticipated to enhance the EL device performance.

To evaluate whether gridization, akin to arylmethylation, can enhance the horizontal dipole orientation ratio ($\Theta_{//}$) of the emitters and thereby improve light outcoupling efficiency in electroluminescent devices, angle-dependent p-polarized photoluminescence spectra were measured for the three emitters embedded in a common CBP host. As shown in Fig. 2c, PXZ-TRZ exhibits a $\Theta_{//}$ of 74%. As expected, arylmethylation increases this value to 77% in DSFPXZ-TRZ, consistent with our previous findings.[36] Upon gridization, the $\Theta_{//}$ further increases to 83% for AG-PXZ-TRZ, likely due to the increased aspect ratio of the emissive molecule conferred by the rigidified grid-like structure.[40] As the solvent polarity increases from apolar toluene to polar THF, the emission peaks of these emitters red-shift by 53–73 nm, indicating a pronounced bathochromic effect (Fig. S12). Moreover, both compounds of AG-PXZ-TRZ and DSFPXZ-TRZ exhibit a progressive enhancement in PL intensity with increasing water content, consistent with aggregation-induced emission (AIE) behaviour (Fig. S13). These results indicate that the gridization, akin to arylmethylation, preserves the AIE characteristics of the emitter.[36]

Furthermore, organic semiconductors are highly susceptible to degradation by reactive oxygen species (ROS) such as superoxide anions (O_2^-), singlet oxygen ($^1O_2$), and hydroxyl radicals ($OH^•$).[49] This oxidative process introduces carrier traps and quenching centers, which adversely impact the electrical performance and operational stability of the resulting devices. To impose more rigorous aging conditions, ozone is introduced as an external oxidative stressor. Amorphous spin-coated films are aged in a fully dark, enclosed environment by exposure to ozone generated at 200 mg h^{-1} with an air flow rate of 1 L min^{-1} for durations ranging from 0 to 210 min.[50] With increasing exposure time, the PL spectra (Fig. 2d) of PXZ-TRZ exhibit a pronounced decrease in emission intensity accompanied by a gradual blue shift of the maximum emission wavelength, resulting in a marked displacement of the CIE coordinates (Fig. S14b). In contrast, DSFPXZ-TRZ (Fig. S14a) and AG-PXZ-TRZ (Fig. 2e) display significantly lower photoluminescence attenuation under identical conditions. Unlike PXZ-TRZ, DSFPXZ-TRZ shows an initial blue shift followed by a red shift after 150 min, which likely arises from conjugation chain scission and low-energy defect states induced by ozone and other reactive oxygen species. Remarkably, AG-PXZ-TRZ retains stable emission intensity and color purity even after 210 min of exposure (Fig. S14d), as evidenced by its persistent yellow luminescence under UV illumination (Fig. 2f). Ozone, as a strong oxidant, readily reacts with carbon–carbon double bonds and electron-rich motifs in organic semiconductors, disrupting conjugation and impairing optoelectronic performance. Introducing bulky steric units adjacent to the reactive sites creates a steric shielding effect that hinders the approach of ozone to the reaction centers. This strategy preserves the highly delocalized π-conjugated framework of AG-PXZ-TRZ and retains its optoelectronic properties with minimal ozone-induced degradation, thereby imparting excellent ozone-aging resistance.

Theoretical calculations

To elucidate the structural and electronic characteristics of the luminescent molecules, ground-state geometries were optimized using density functional theory (DFT) at the B3LYP/6-31G(d) level. As illustrated in Fig. S15, the dihedral angles between the electron-donating phenoxazine unit and the adjacent benzene acceptors (D–A) in PXZ-TRZ, DSFPXZ-TRZ and AG-PXZ-TRZ are 74°, 70° and 86°, respectively. The largest torsion observed in AG-PXZ-TRZ underscores the impact of gridization in enhancing molecular distortion, thereby promoting the greatest spatial separation of the HOMO and LUMO and facilitating a reduced ΔE_{ST}. Electrostatic potential analyses further reveal that the incorporation of the nanogrid framework exerts negligible influence on the overall electrostatic potential distribution. The HOMOs of the emitter molecules are predominantly delocalized over the phenoxazine units, while the LUMOs remain confined to the triazine moiety (Fig. 3). In AG-PXZ-TRZ, the non-conjugated fluorene segments function as steric shields encasing the emissive core, thereby mitigating intermolecular interactions. The observed enhancement in transition oscillator strengths (f) can be attributed to the increased π-conjugation within the AG-PXZ-TRZ molecule induced by gridization.[51] As a result, markedly enhanced radiative decay rates are expected, underscoring the effectiveness of this molecular design strategy.

The natural transition orbital (NTO) analysis reveals that, akin to PXZ-TRZ, the electronic transitions in both DSFPXZ-TRZ and AG-PXZ-TRZ predominantly occur between the donor and

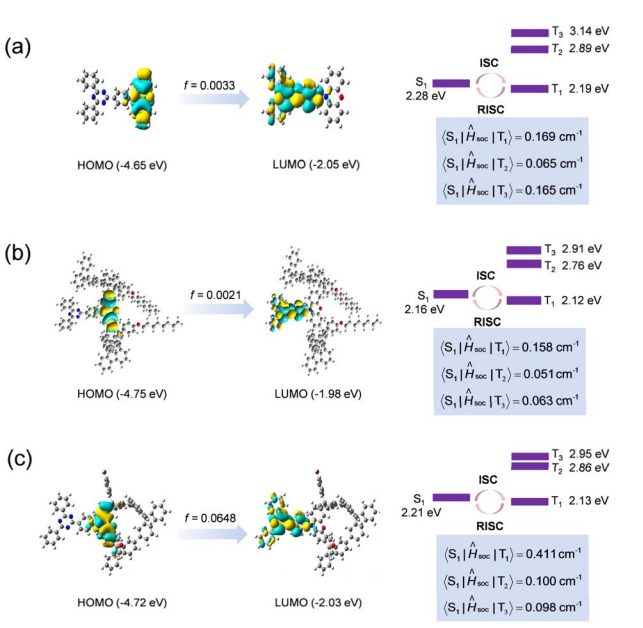

Fig. 3 HOMO/LUMO distribution, oscillator strengths, state levels, and SOC constants of (a) PXZ-TRZ, (b) DSFPXZ-TRZ and (c) AG-PXZ-TRZ.

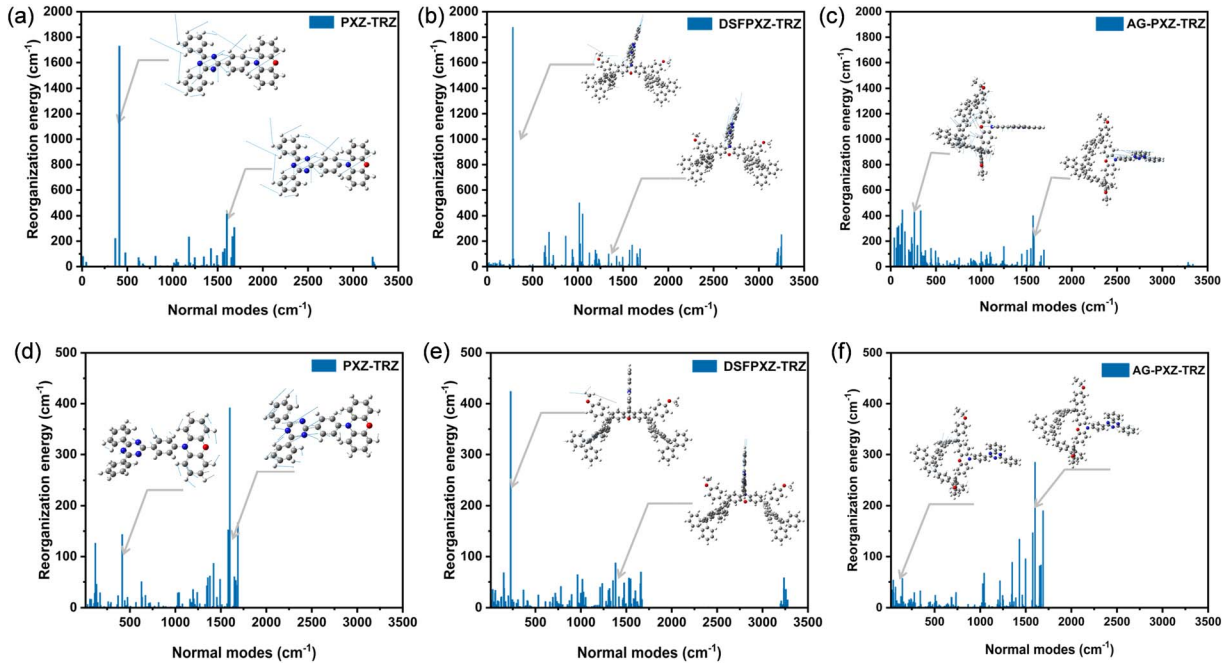

Fig. 4 The reorganization energy contribution from every vibration mode to the relaxation of S_1 of (a) PXZ-TRZ, (b) DSFPXZ-TRZ and (c) AG-PXZ-TRZ molecules in toluene; (d) PXZ-TRZ, (e) DSFPXZ-TRZ and (f) AG-PXZ-TRZ in films.

acceptor moieties (Fig. S16–S18). The S_1, S_2, and T_1 states of AG-PXZ-TRZ exhibit pronounced charge-transfer (CT) character, exceeding 85%, consistent with the typical CT nature of TADF molecules. Calculated excitation energies further reveal that PXZ-TRZ exhibits minimal variation in energy levels between the solution and film, yet displays an elevated S_1 state in the solid-state, thereby inducing an enhanced ΔE_{ST} in the film. In contrast, AG-PXZ-TRZ consistently displays a smaller ΔE_{ST}, which can be attributed to its increased torsional distortion. Additionally, it can be seen from Fig. S19 that the excitation energies of the molecules exhibit marked environmental dependence. Specifically, upon arylmethylation, the S_1 state excitation energy of the molecule decreases, while the T_1 state energy remains largely unaffected in the film state, culminating in a reduced ΔE_{ST} of DSFPXZ-TRZ.[52] This similar trend is also observed in gridization for AG-PXZ-TRZ, underscoring a similar modulation of excited-state energetics. Such small ΔE_{ST} would lead to an effective RISC process and benefit the utilizations of triplet excitons. Moreover, the A-shaped nanogrid-based emitter AG-PXZ-TRZ exhibits markedly enhanced spin–orbit coupling (SOC) between S_1 and the triplet states (T_1 and T_2), relative to both PXZ-TRZ and DSFPXZ-TRZ, with SOC values increasing from 0.158 to 0.411 cm^{-1} (S_1–T_1) and from 0.051 to 0.100 cm^{-1} (S_1–T_2), respectively. Although T_2 and T_3 possess pronounced ^{3}LE character, the magnitude of SOC is governed not only by the LE nature of the triplet states but also by the orbital composition and energetic proximity of the coupled singlet–triplet pair. The S_1 and T_1 states exhibit mixed HLCT character, combining sufficient orbital overlap with partial charge separation, which leads to enhanced spin–orbital interaction compared with pure LE or CT states. Moreover, the small S_1–T_1 energy gap increases wavefunction overlap and strengthens state-to-state coupling, resulting in a larger SOC matrix element for S_1–T_1 than for S–T_2 or S_1–T_3. These features collectively account for the dominant SOC observed between S_1 and T_1. This pronounced improvement is anticipated to facilitate efficient RISC, consistent with the experimental observations above, thereby augmenting exciton utilization efficiency and advancing overall device performance.

To quantitatively characterize geometric changes in the overall molecule between excited states, the root mean square displacement (RMSD) of excited-state geometries in *n*-hexane was computed using Multiwfn 3.8. A large RMSD value indicates significant conformational differences between excited states, a larger structural modification required for molecular transitions, and greater energy dissipation. Conversely, a small RMSD value suggests the opposite. As shown in Fig. S20, AG-PXZ-TRZ exhibits increased geometric deviations between S_0 and S_1 relative to PXZ-TRZ and DSFPXZ-TRZ. Specifically, the RMSD between S_0 and S_1 is 0.4736 Å for PXZ-TRZ and 0.4196 Å for DSFPXZ-TRZ, whereas AG-PXZ-TRZ displays a slightly higher value of 0.6166 Å. Notably, Fig. S20 reveals that these larger deviations for AG-PXZ-TRZ predominantly originate from the flexible alkyl chains rather than the rigid molecular backbone. However, the AG-PXZ-TRZ molecule exhibits a smaller RMSD between the S_1 and T_1 states, indicating a smaller conformational change between these states. This suppression of structural relaxation likely arises from increased molecular rigidity and steric hindrance induced by gridization. This suggests that the reorganization energy changes during the exciton ISC and RSIC processes are relatively minor, and the non-radiative

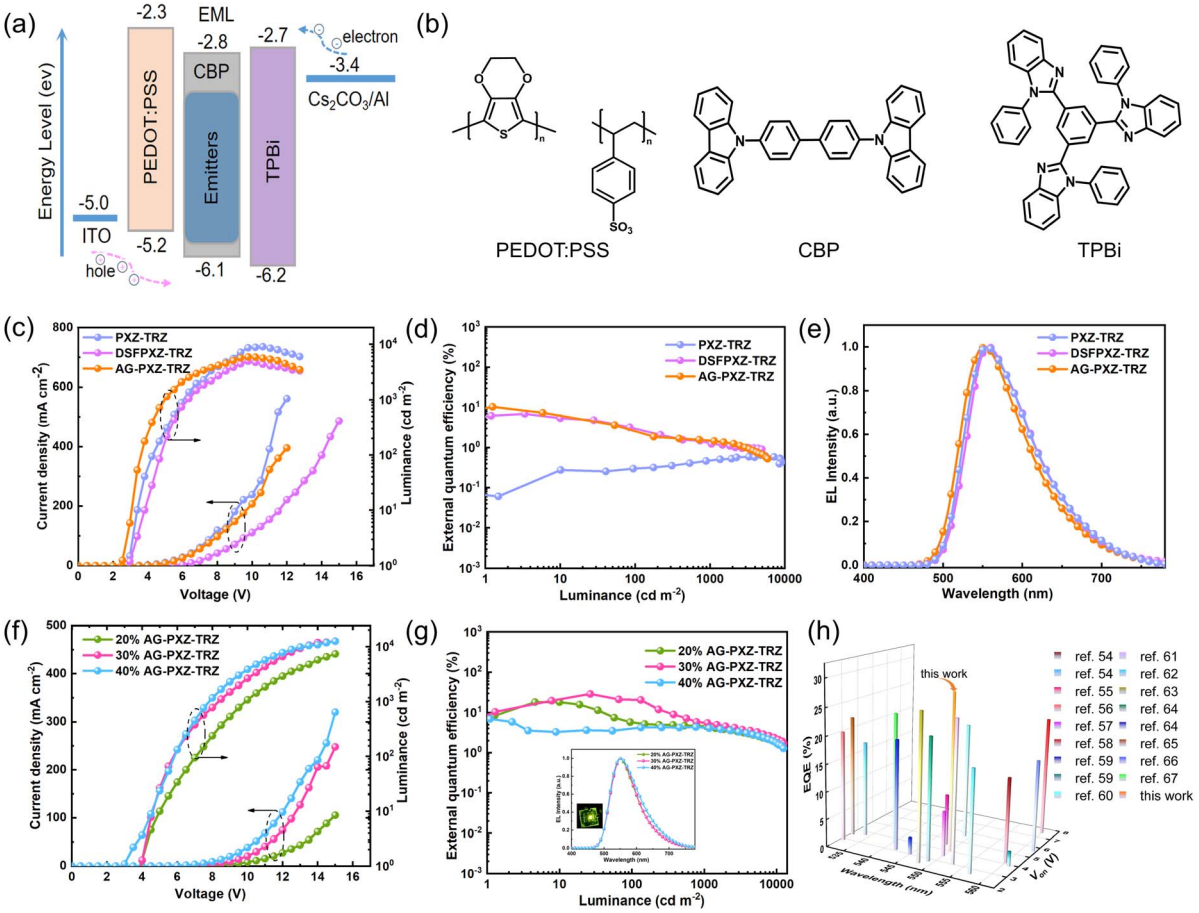

Fig. 5 (a) Energy level diagram and (b) material chemical structures of the devices. (c) Current density–voltage–luminance (*J*–*V*–*L*) curves of non-doped devices; (d) external quantum efficiency *versus* luminance; EL spectra of (e) PXZ-TRZ, DSFPXZ-TRZ and AG-PXZ-TRZ; (f) and (g) current density–voltage–luminance (*J*–*V*–*L*) curves and external quantum efficiency *versus* luminance of AG-PXZ-TRZ at different doping ratios (inset shows the EL spectra and a photo of the device); (h) external quantum efficiency and turn-on voltage diagrams of devices as solution-processed OLEDs with yellow-green TADF emitters.

energy dissipation pathways are hindered, potentially leading to enhanced fluorescence efficiency.[53]

To further investigate the non-radiative energy dissipation processes associated with gridization, we calculated the reorganization energies of these emitters in their toluene solutions and films. The results reveal that vibrational modes within the intermediate frequency range (200–1500 cm^{-1}) contribute significantly to the reorganization energy. As illustrated in Fig. 4, the reorganization energies of the emissive molecules in thin-film states are notably lower than those in solution states within this frequency range, indicating effective suppression of molecular vibrations in the solid state. Compared to PXZ-TRZ, incorporation of the 9-aryl-9-fluorenyl substituents in DSFPXZ-TRZ markedly enhances vibrational coupling, which is likely to facilitate non-radiative energy dissipation and result in an increased k_{nr}. Notably, the reorganization energy of AG-PXZ-TRZ remains consistently lower than that of PXZ-TRZ and DSFPXZ-TRZ, regardless of its state—whether in solutions or films. This observation underscores the role of gridization in suppressing vibration-induced non-radiative energy dissipation, consistent with prior analyses, and thus offers a compelling strategy for advancing OLED performance.

Device performance

Cyclic voltammetry (CV) experiments were further performed to elucidate the electrochemical characteristics and estimate the HOMO and LUMO energy levels relevant for OLED fabrication (Fig. S8). The HOMO levels are determined to be −5.60 eV and −5.55 eV for AG-PXZ-TRZ and DSFPXZ-TRZ, respectively. From the onset of the reduction wave, the LUMO energy levels are calculated to be −3.39 eV and −3.25 eV, respectively. The elevated HOMO level and suitably aligned LUMO of AG-PXZ-TRZ are expected to facilitate efficient charge injection and recombination, which is crucial to improving the device performance of OLEDs.

To evaluate the potential of AG-PXZ-TRZ in solution-processed OLEDs, devices with the configuration ITO/PEDOT:PSS (30 nm)/EML/TPBI/Cs_2CO_3/Al were fabricated *via* spin-coating. The corresponding energy-level alignment of the device components is illustrated in Fig. 5a. In this architecture, ITO and Al function as the anode and cathode, respectively. PEDOT:PSS (poly(3,4-ethylenedioxy-thiophene):poly(styrene sulfonate)) and Cs_2CO_3 serve as hole- and electron-injection layers, while TPBI acts as the electron-transporting layer. First,

to probe the intrinsic emissive properties of AG-PXZ-TRZ, non-doped OLEDs were fabricated using pure AG-PXZ-TRZ as the emission layer. The resulting devices exhibit a low turn-on voltage (V_{on}) of 3.0 V and achieve a maximum luminance (L_{max}) exceeding 5800 cd m^{-2} (Fig. 5c). Notably, the devices deliver a maximum current efficiency (CE_{max}) of 32.1 cd A^{-1} and an external quantum efficiency (EQE_{max}) of 10.4%. For comparison, OLEDs based on the acyclic analogue DSFPXZ-TRZ exhibit a CE_{max} of 20.8 cd A^{-1} and an EQE_{max} of 6.92%, while those incorporating the parent emitter PXZ-TRZ show markedly lower performance, with a CE_{max} of 1.84 cd A^{-1} and an EQE_{max} of 0.65%. The device incorporating nanogrid AG-PXZ-TRZ exhibits a markedly enhanced external quantum efficiency—more than tenfold higher than that of the control emitter—primarily due to its superior film-forming properties and suppressed exciton quenching. The EL spectrum of AG-PXZ-TRZ peaks at 552 nm, exhibiting a red shift of 13 nm relative to its PL in the solid state. Similarly, DSFPXZ-TRZ exhibits an EL peak at 556 nm, exhibiting a redshift of 6 nm compared to its PL spectrum. In contrast, PXZ-TRZ displays a more significant redshift of 23 nm, with PL and EL maxima observed at 532 nm and 555 nm, respectively. The relatively smaller shift observed for AG-PXZ-TRZ suggests that the nanogrid architecture effectively suppresses intermolecular interactions, thereby minimizing exciton energy loss during device operation.

For device optimization, these emitters were incorporated as dopants into the CBP host at concentrations of 20 wt%, 30 wt%, and 40 wt%, serving as the EML. The resulting OLEDs exhibit relatively low turn-on voltages, ranging from 3.0 to 4.5 V, with a clear downward trend as the dopant concentration increases (Fig. 5f, S21 and Table S1). Among these, devices incorporating AG-PXZ-TRZ consistently show lower turn-on voltages relative to their analogues. Notably, the device incorporating a 30 wt% nanogrid emitter AG-PXZ-TRZ achieves state-of-the-art performance for solution-processed yellow-green TADF OLEDs (Fig. 5h),[54–67] with a maximum luminance of 12 000 cd m^{-2}, an EQE_{max} of 28.9%, and a CE_{max} of 87.2 cd A^{-1}. By contrast, the parent emitter PXZ-TRZ and its non-grid analogue DSFPXZ-TRZ exhibit significantly reduced device performance, with the sole exception of the emission brightness in the PXZ-TRZ-based device. Specifically, the EQE_{max} of PXZ-TRZ and DSFPXZ-TRZ reach 2.97% and 15.4%, respectively, while their corresponding CE_{max} values are 8.78 cd A^{-1} and 46.7 cd A^{-1}. These results provide compelling evidence for the efficacy of our gridization strategy in the rational design of high-performance TADF emitters.

Conclusions

In summary, this work establishes molecular gridization as a robust and versatile strategy for constructing stable, efficient, and solution-processable TADF macrocycles. The macrocyclic nanogrid architecture unites rigidity, spatial confinement, and optimized electronic coupling within a single molecular framework, thereby enhancing solution processability, suppressing aggregation, lowering reorganization energy, and reinforcing spin-conversion dynamics while simultaneously improving ozone resistance. These cooperative effects minimize exciton loss and direct horizontal dipole alignment, resulting in accelerated radiative decay (3.1×) and reverse intersystem crossing (5.5×) relative to the parent emitter PXZ-TRZ. The corresponding solution-processed OLEDs achieve an external quantum efficiency of 28.9%, markedly outperforming both PXZ-TRZ and the non-grid analogue DSFPXZ-TRZ. Beyond simplifying macrocycle synthesis, gridization transforms donor design into a modular and predictive approach for controlling excitonic behavior in organic semiconductors. The nanogrid concept thus provides a universal molecular blueprint for high-performance organic emitters and offers a promising foundation for next-generation optoelectronic systems, including organic lasers, photodetectors, and upconversion devices.

Author contributions

Q. F. and A. Z. contributed equally to this work. Q. F., Z. W., L. X. and W. H. devised, planned, and supervised the project and evaluated the data and results. A. Z., K. G., Y. Z., Y. C. and H. W. performed material synthesis. Q. F., A. Z., Q. H., J. M., H. L., M. Y. and M. X. performed characterizations of the materials. Y. P. conducted calculations. X. B., A. Z. and G. X. performed and supervised device fabrication and characterization. All authors contributed to writing and reviewing the manuscript.

Conflicts of interest

There are no conflicts to declare.

Data availability

The data that supports the findings of this are available in the supplementary information (SI) of this article. Supplementary information is available. See DOI: https://doi.org/10.1039/d5sc08430j.

Acknowledgements

This work was financially supported by the National Key R&D Program of China (2024YFB3612600), the National Natural Science Foundation of China (22375100, 22275098 and 62288102), the Basic Research Program of Jiangsu (BK20243057), and the Project of State Key Laboratory of Flexible Electronics (GZR2024010016 and GDX2022010005). The authors are grateful to Ideaoptics Co., Ltd for the technical support of the R1-OLED angular resolution spectrometer test system.

Notes and references

1 I. Sim, K. Choi, Y. Baek, J. H. Choi, J. Jo, J. Yeom, B. Kim, Y. Cho, H. Lee, H. Bang, J.-H. Han, D. H. Park, J. Kim and K. Lee, *Nat. Rev. Electr. Eng.*, 2025, **2**, 634–650.
2 Z. Zhang, W. Wang, Y. Jiang, Y.-X. Wang, Y. Wu, J.-C. Lai, S. Niu, C. Xu, C.-C. Shih and C. Wang, *Nature*, 2022, **603**, 624–630.

3 J. Shen and Q. Zhu, *Mater. Res. Bull.*, 2022, **156**, 111987.
4 J. Ye, D. Gaur, C. Mi, Z. Chen, I. L. Fernández, H. Zhao, Y. Dong, L. Polavarapu and R. L. Z. Hoye, *Chem. Soc. Rev.*, 2024, **53**, 8095–8122.
5 C. W. Tang and S. A. VanSlyke, *Appl. Phys. Lett.*, 1987, **51**, 913–915.
6 Future Market Insights, OLED Market Size and Share Forecast Outlook 2025 to 2035, https://www.futuremarketinsights.com/reports/oled-market, accessed 17 Sept 2025.
7 Y. Liu, Y. Dong, T. Zhu, D. Ma, A. Proppe, B. Chen, C. Zheng, Y. Hou, S. Lee, B. Sun, E. H. Jung, F. Yuan, Y.-k. Wang, L. K. Sagar, S. Hoogland, F. P. García de Arquer, M.-J. Choi, K. Singh, S. O. Kelley, O. Voznyy, Z.-H. Lu and E. H. Sargent, *J. Am. Chem. Soc.*, 2021, **143**, 15606–15615.
8 Y.-K. Wang, H. Wan, S. Teale, L. Grater, F. Zhao, Z. Zhang, H.-W. Duan, M. Imran, S.-D. Wang, S. Hoogland and L.-S. Liao, *Nature*, 2024, **629**, 586–591.
9 X. Jiao, Y. Wang, R. Zhu, Y. Chen, J. Pan, Z. Lu, X.-C. Hang, Z. Sun and W. Huang, *FlexMat*, 2025, **2**, 442–451.
10 Y. Khan, S. Hwang, R. Braveenth, Y. H. Jung, B. Walker and J. H. Kwon, *Nat. Commun.*, 2022, **13**, 1801.
11 H. Piwoński, S. Nozue, H. Fujita, T. Michinobu and S. Habuchi, *Nano Lett.*, 2021, **21**, 2840–2847.
12 J.-P. Liu, L. Chen, L. Zhao, C.-Y. Tong, S.-M. Wang, S.-Y. Shao and L.-X. Wang, *Chin. J. Polym. Sci.*, 2023, **41**, 802–810.
13 T. C. Lovell, Z. R. Garrison and R. Jasti, *Angew. Chem., Int. Ed.*, 2020, **59**, 14363–14367.
14 Q. Feng, S. Zhu, B. Wang, F. Yu, H. Li, M. Yu, M. Xu and L. Xie, *Adv. Funct. Mater.*, 2024, **34**, 2312622.
15 D. Sun, E. Duda, X. Fan, R. Saxena, M. Zhang, S. Bagnich, X. Zhang, A. Köhler and E. Zysman-Colman, *Adv. Mater.*, 2022, **34**, 2110344.
16 J. Kang, H. L. Lee, S. O. Jeon, H. J. Bae, S. C. Kim, S. Han and J. Y. Lee, *Adv. Sci.*, 2024, **11**, 2405604.
17 L. Li, T. Huang, Y. Xu, Y. Qu, W. Cui, L. Xu, C. Li and Y. Wang, *Angew. Chem., Int. Ed.*, 2025, **64**, e202504002.
18 G. Meng, J. Zhou, T. Huang, H. Dai, X. Li, X. Jia, L. Wang, D. Zhang and L. Duan, *Angew. Chem., Int. Ed.*, 2023, **62**, e202309923.
19 S. Oda, W. Kumano, T. Hama, R. Kawasumi, K. Yoshiura and T. Hatakeyama, *Angew. Chem., Int. Ed.*, 2021, **60**, 2882–2886.
20 M. Ball, B. Zhang, Y. Zhong, B. Fowler, S. Xiao, F. Ng, M. Steigerwald and C. Nuckolls, *Acc. Chem. Res.*, 2019, **52**, 1068–1078.
21 X. N. Han, Y. Han and C. F. Chen, *Angew. Chem., Int. Ed.*, 2025, **64**, e202424276.
22 S. Izumi, H. F. Higginbotham, A. Nyga, P. Stachelek, N. Tohnai, P. d. Silva, P. Data, Y. Takeda and S. Minakata, *J. Am. Chem. Soc.*, 2020, **142**, 1482–1491.
23 D. Chang, X. Xiao, D. An, R. Zhang, X. Song, Y. Liu, Y. Zhao and X. Lu, *Aggregate*, 2023, **4**, e380.
24 Y. Segawa, D. R. Levine and K. Itami, *Acc. Chem. Res.*, 2019, **52**, 2760–2767.
25 R. Jasti, J. Bhattacharjee, J. B. Neaton and C. R. Bertozzi, *J. Am. Chem. Soc.*, 2008, **130**, 17646–17647.
26 X.-N. Han, Y. Han and C.-F. Chen, *Angew. Chem., Int. Ed.*, 2025, **64**, e202424276.
27 J. K.-H. Wong, M. H. Todd and P. J. Rutledge, *Molecules*, 2017, **22**, 200.
28 P. Ceroni, A. Y. Lebedev, E. Marchi, M. Yuan, T. V. Esipova, G. Bergamini, D. F. Wilson, T. M. Busch and S. A. Vinogradov, *Photochem. Photobiol. Sci.*, 2011, **10**, 1056–1065.
29 N. Pan, Z. Wu, H. Hu, L. Yao, J. Xie, K. Zhu and C. Jia, *Sci. China Chem.*, 2025, **68**, 5032–5038.
30 J. Xiao, D. Liu, Y. Fu, W. Xie, Y. Mu, J.-X. Chen, Z. Ye, S. Ji, Y. Huo and S.-J. Su, *Angew. Chem., Int. Ed.*, 2025, **64**, e202415680.
31 X. Ban, Q. Cao, W. Zhang, W. Bian, C. Yang, J. Wang, Y. Qian, H. Xu, C. Tao and W. Jiang, *Chem. Sci.*, 2024, **15**, 18196–18206.
32 M. Du, Y. Chen, M. Mai, T. Fan, Q. Jin, Y. Zhang and L. Duan, *FlexMat*, 2024, **1**, 46–53.
33 A. Zhou, Z. Sun and L. Sun, *Innovation*, 2024, **5**, 100662.
34 T. Yang, Y. Tang, Y. Wei, L. Xie and W. Huang, *Acc. Chem. Res.*, 2025, 1748–1751.
35 Y. Wang, L. Dong, S. Li, Y. Feng, X. Ge, X. Han, C. Liu, Y. Wei, X. Cheng and L. Xie, *J. Phys. Chem. Lett.*, 2025, **16**, 3888–3903.
36 Q. Feng, Y. Qian, H. Wang, W. Hou, X. Peng, S. Xie, S. Wang and L. Xie, *Adv. Opt. Mater.*, 2022, **10**, 2102441.
37 Y. K. Wang, Z. C. Yuan, G. Z. Shi, Y. X. Li, Q. Li, F. Hui, B. Q. Sun, Z. Q. Jiang and L. S. Liao, *Adv. Funct. Mater.*, 2016, **26**, 1375–1381.
38 Q. Feng, S. Xie, K. Tan, X. Zheng, Z. Yu, L. Li, B. Liu, B. Li, M. Yu, Y. Yu, X. Zhang, L. Xie and W. Huang, *ACS Appl. Polym. Mater.*, 2019, **1**, 2441–2449.
39 Z. Zhao, C. Zeng, X. Peng, Y. Liu, H. Zhao, L. Hua, S.-J. Su, S. Yan and Z. Ren, *Angew. Chem., Int. Ed.*, 2022, **61**, e202210864.
40 F. Tenopala-Carmona, O. S. Lee, E. Crovini, A. M. Neferu, C. Murawski, Y. Olivier, E. Zysman-Colman and M. C. Gather, *Adv. Mater.*, 2021, **33**, 2100677.
41 X. Li, L. Yan, S. Liu, S. Wang, J. Rao, L. Zhao, H. Tian, J. Ding and L. Wang, *Angew. Chem., Int. Ed.*, 2023, **62**, e202300529.
42 Z. Liu, J. Rao, S. Zhu, B. Wang, F. Yu, Q. Feng and L. Xie, *Acta Chim. Sin.*, 2023, **81**, 820–835.
43 Y. Xiang, S. Gong, Y. Zhao, X. Yin, J. Luo, K. Wu, Z.-H. Lu and C. Yang, *J. Mater. Chem. C*, 2016, **4**, 9998–10004.
44 S. L. Zhang, Y. Z. Shi, K. Wang, X. C. Fan, J. Yu, X. M. Ou and X. H. Zhang, *Mater. Today Energy*, 2021, **20**, 100581.
45 Y. Xin, Y. Zhu, R. Chi, C. Duan, P. Yan, C. Han and H. Xu, *Adv. Mater.*, 2023, **35**, 2304103.
46 Y. Ren, S. Yang and Y. Xu, *Acc. Chem. Res.*, 2025, **58**, 474–487.
47 H. Tanaka, K. Shizu, H. Miyazaki and C. Adachi, *Chem. Commun.*, 2012, **48**, 11392–11394.
48 M. Yu, X. Jia, D. Lin, X. Du, D. Jin, Y. Wei, L. Xie and W. Huang, *Front. Chem.*, 2021, **9**, 717892.
49 L. Yuan, Y. Huang, X. Chen, Y. Gao, X. Ma, Z. Wang, Y. Hu, J. He, C. Han, J. Li, Z. Li, X. Weng, R. Huang, Y. Cui, L. Li and W. Hu, *Nat. Mater.*, 2024, **23**, 1268–1275.
50 H. Li, M. Yu, Y. Li, M. Luo, J. Ma, Y. Zhang, Y. Wang, Y. Zhang, Y. Ma, L. Bai, Q. Bao, J. Gu, J. a. Liu, J. Lin,

X. Zhang, C. Li, M. Xu, Q. Feng and L. Xie, *Chem. Eng. J.*, 2024, 156598.
51 G. Meng, H. Dai, J. Zhou, T. Huang, X. Zeng, Q. Wang, X. Wang, Y. Zhang, T. Fan, D. Yang, D. Ma, D. Zhang and L. Duan, *Chem. Sci.*, 2023, **14**, 979–986.
52 Y. Liang, M. Xu, Y. Chi, T. Liang, X. Jiang, J. Wang, Y. Pan and B. Yang, *Chem. Phys. Lett.*, 2023, **811**, 140257.
53 M. Xing, G. Chen, S. Wang, X. Yin, J. Liu, Z. Xue, N. Li, J. Miao, Z. Huang and C. Yang, *Adv. Funct. Mater.*, 2025, **35**, 2414635.
54 G. Xie, X. Li, D. Chen, Z. Wang, X. Cai, D. Chen, Y. Li, K. Liu, Y. Cao and S. J. Su, *Adv. Mater.*, 2016, **28**, 181–187.
55 S. Y. Lee, T. Yasuda, H. Komiyama, J. Lee and C. Adachi, *Adv. Mater.*, 2016, **28**, 4019–4024.
56 H.-Y. Yang, C.-J. Zheng, M. Zhang, J.-W. Zhao, P.-L. Zhong, H. Lin, S.-L. Tao and X.-H. Zhang, *Org. Electron.*, 2019, **73**, 36–42.
57 S. Gong, J. Luo, Z. Wang, Y. Li, T. Chen, G. Xie and C. Yang, *Dyes Pigm.*, 2017, **139**, 593–600.
58 M. I. Alam, M. R. Nagar, J.-H. Jou and S. Vaidyanathan, *Chem. Mater.*, 2024, **36**, 8649–8662.
59 C. Si, D. Sun, T. Matulaitis, D. B. Cordes, A. M. Slawin and E. Zysman-Colman, *Sci. China Chem.*, 2024, **67**, 1613–1623.
60 Y. Long, X. Chen, H. Wu, Z. Zhou, S. Sriram Babu, M. Wu, J. Zhao, M. P. Aldred, S. Liu, X. Chen, Z. Chi, J. Xu and Y. Zhang, *Angew. Chem., Int. Ed.*, 2021, **60**, 7220–7226.
61 Y. Liu, Y. Xie, L. Hua, X. Tong, S. Ying, Z. Ren and S. Yan, *CCS Chem.*, 2023, **5**, 1005–1017.
62 R. Dong, D. Liu, J. Li, M. Ma, Y. Mei, D. Li and J. Jiang, *Mater. Chem. Front.*, 2022, **6**, 40–51.
63 L. Chen, J. Lv, S. Wang, S. Shao and L. Wang, *Adv. Opt. Mater.*, 2021, **9**, 2100752.
64 Y. Liu, L. Hua, S. Yan and Z. Ren, *Nano Energy*, 2020, **73**, 104800.
65 C. Y. Kim, C. Lee, H. J. Kim, J. Hwang, M. Godumala, J.-E. Jeong, H. Y. Woo, M. J. Cho, S. Park and D. H. Choi, *J. Mater. Chem. C*, 2020, **8**, 6780–6787.
66 F. Wang, W. Qiu, J. Zeng, P. Yuan, W. Zong, W. Wu, Y. Liu, S. Xu, S.-J. Su and S. Cao, *J. Mater. Chem. C*, 2020, **8**, 4469–4476.
67 Y. Chiba, K. Hoshi, G. Yamda, H. Nemma, R. Otomo, D. Jiang, N. Meguro, H. Katagiri, J. Kido and H. Sasabe, *Adv. Funct. Mater.*, 2025, **35**, 2425759.